Physics of Fluids

Explosive boiling induced fast transportation of Leidenfrost droplet to target location

Cite as: Phys. Fluids **34**, 053322 (2022); https://doi.org/10.1063/5.0091303
Submitted: 14 March 2022 • Accepted: 05 May 2022 • Accepted Manuscript Online: 07 May 2022 • Published Online: 25 May 2022

Chunlei Cao (曹春蕾), Xiaojing Ma (马骁婧), Jinliang Xu (徐进良), et al.

Physics of Fluids ARTICLE scitation.org/journal/phf

Explosive boiling induced fast transportation of Leidenfrost droplet to target location

Cite as: Phys. Fluids **34**, 053322 (2022); doi: 10.1063/5.0091303
Submitted: 14 March 2022 · Accepted: 5 May 2022 ·
Published Online: 25 May 2022

Chunlei Cao (曹春蕾),[1] Xiaojing Ma (马骁婧),[1,2] Jinliang Xu (徐进良),[1,2,a)] Haiwang Li (李海旺),[3] and Guanglin Liu (刘广林)[1]

AFFILIATIONS

[1]Key Laboratory of Power Station Energy Transfer Conversion and System of Ministry of Education, North China Electric Power University, Beijing 102206, People's Republic of China
[2]Beijing Key Laboratory of Multiphase Flow and Heat Transfer for Low Grade Energy Utilization, North China Electric Power University, Beijing 100026, People's Republic of China
[3]Beihang University, National Key Laboratory of Science and Technology on Aero Engine Aerothermo, Beijing 100191, People's Republic of China

[a)]Author to whom correspondence should be addressed: xjl@ncepu.edu.cn

ABSTRACT

Leidenfrost droplet possesses ultra-low flow resistance, but it is challenging to obtain large thrust force for fast transportation and regulate the direction of droplet motion. Here, for the first time, we demonstrate a novel mechanism for the control of droplet dynamics by explosive boiling. Our system consists of two surfaces that have different functions: a smooth surface running in the Leidenfrost state for droplet levitation and a skirt ring edge surface (SRES) as an explosive boiling trigger. For droplet-wall collision with SRES, micro/nanoscale roughness not only enhances energy harvesting from the skirt ring to the droplet due to increased radiation heat transfer but also provides nucleation sites to trigger explosive boiling. The symmetry breaking of explosive boiling creates a thrust force that is sufficient to propel the droplet. The suppression of the thrust force relative to the inertia force regulates the droplet trajectory as it passes through a target location. We show orbit lines passing through a focusing spot that is ∼1% of the Leidenfrost surface area around its center with a maximum traveling speed of ∼85 cm/s, which is ∼2 times of that reported in the literature. The scale law analysis explains the droplet size effect on the self-propelling droplet dynamics. Our work is attractive for applications under the conditions of the required traveling speed and direction of the droplet.

I. INTRODUCTION

Considering a droplet on a heated surface, when the surface temperature exceeds a critical value, a vapor layer beneath the droplet occurs to decrease the evaporation rate of the droplet, which is called the Leidenfrost phenomenon.[1] This phenomenon has received much interest due to various applications, including energy conversion,[2] drag reduction,[3] drug delivery,[4,5] and micro/nanotechnologies.[6–8] Spray cooling is effective to dissipate high heat flux from a surface, but high heater surface temperature may trigger Leidenfrost to make the cooling ineffective.[9] To increase energy conversion efficiency for heat engines, vapor temperature at the turbine inlet is as high as 620–700 °C,[10] under which the Leidenfrost point should be avoided in heat exchangers. Various methods including micro/nanostructured surface,[11–13] wettability control,[14] oscillation augmentation,[15] and electric-field-augmentation[16] are used to delay the Leidenfrost transition temperature.

A Leidenfrost droplet is not stable above a hot surface to display random motion. Control of droplet dynamics is useful for various applications such as micro/nanofluidics,[17,18] water collection,[19,20] and drug delivery,[4,5,21] but it is a challenging task. The available methods use micro/nanotextured structures,[22–26] wettability gradient,[27–29] and temperature gradient[30] to create imbalance force across the two sides of the droplet to propel its motion. The saw-tooth structure in the ∼μm or ∼mm scale belongs to one of these families.[23,25,26] At sufficiently high temperature, vapor generates in a saw-tooth structure to prevent direct contact between the liquid and solid. The complicated interaction among droplet (liquid), vapor, and solid involves several effects which influence droplet dynamics, including viscous force in the vapor layer,[31] Marangoni effect due to non-uniform temperature,[32,33] and different vapor pressure forces acting on vertical and inclined walls of the saw-tooth structure.[23,34,35] Jia *et al.*[23] noted

three modes of advancing, receding, or even stationary droplet due to non-uniform vapor pressure distribution in the saw-tooth structure.

There are several issues to control droplet dynamics. First, the motion direction becomes uncertain when operating conditions are changed. For example, the change of heater temperature may alter the motion direction (advancing, receding, or stationary).[23] Second, the widely studied saw-tooth structure is only effective for droplet larger than the tooth width. A droplet may be clamped in a saw-tooth for the droplet smaller than the saw-tooth width.[31] Third, the maximum traveling speed of droplet is reported as ∼38 cm/s.[36] The nanostructure surface may not be able to sustain long term operation at high temperatures.[37]

The phase change from liquid to vapor consists of two modes of evaporation and boiling. The former refers to mass transfer from liquid to vapor due to the temperature gradient within the liquid boundary layer, while the latter refers to bubble nucleation and growth. The homogeneous/heterogeneous nucleation theory dominates the bubble nucleation followed by the bubble growth.[38] Assuming a Leidenfrost droplet levitated above a hot surface, if the droplet does not contain particles or non-condensable gas, boiling shall not occur except that the droplet temperature reaches the temperature limit of $0.8–0.9T_c$ (homogeneous nucleation),[39] where T_c is the critical temperature of the liquid. A Leidenfrost droplet is overheated to store a specific amount of thermal energy.[40] Solid particles or non-condensable gas in the droplet decrease the bubble nucleation temperature, satisfying the heterogeneous nucleation theory.[41] This explains explosive boiling observed in the latter evaporation stage for the dirty droplet.[41] Utaka *et al.*[42] improved the critical heat flux (CHF) of boiling heat transfer in open narrow gaps in a water pool. A method of the interactions between different modes of nucleate boiling and film boiling was investigated.

Here, we create a novel concept for the control of droplet motion. Because nucleate boiling does not occur for a Leidenfrost droplet below the homogeneous nucleation temperature limit, another sidewall surface with a lower temperature than the substrate surface and apparent roughness is introduced to trigger explosive boiling for droplet propulsion. The principle lies in the time-series integration of the elevated Leidenfrost droplet temperature and the surface roughness induced explosive boiling. When a warm droplet contacts the sidewall surface, the rough surface not only enhances radiation heat transfer toward the droplet but also provides sufficient bubble nucleation sites for explosive boiling. The explosive boiling converts a portion of the stored thermal energy of the droplet into kinetic energy, displaying the symmetry-breaking to generate sufficient thrust force for droplet propulsion. The two surfaces have different functions. The Leidenfrost surface levitates the droplet, acting as the transport orbit. The rough skirt ring surface acts as the explosive boiling trigger. We show that the droplet trajectory can be regulated to pass through a focusing region around the Leidenfrost surface center, and the traveling speed of the droplet can be up to ∼85 cm/s, significantly larger than those reported in the literature.

II. CONTROL OF DROPLET DYNAMICS BY EXPLOSIVE BOILING

A. The mixed mode of Leidenfrost and nucleate boiling on two surfaces

Inspired by the rocket launch principle that a high speed of rocket can be caused by hot gas ejection to produce sufficient thrust force, we create a novel concept to control the droplet dynamics. The working principle involves a mixed working mode of Leidenfrost on a substrate and nucleate boiling via the interaction between the droplet and the skirt ring surface. The temperature difference ($T_w - T_r$) and the surface roughness are important to control the droplet motion. Considering droplet evaporation on two smooth surfaces, evaporation time τ is plotted vs temperature T_w, including a nucleate boiling regime A′B′, a transition regime B′A, and a Leidenfrost regime AB [see Fig. 1(a)]. The two surfaces contact with each other, with the substrate temperatures T_A and T_B, correspond to the skirt ring temperatures $T_{A'}$ and $T_{B'}$, respectively. The temperature difference between the two surfaces, $\Delta T = T_w - T_r$, should be large such as ∼90 K to create an effective AB zone for Leidenfrost and A′B′ zone for nucleate boiling. Practically, the large ΔT is difficult to reach. This difficulty can be overcome by introducing the skirt ring roughness, which shifts the evaporation curve from left to right [see the below curve in Fig. 1(b)]. Increasing the wall roughness delays the Leidenfrost transition point.[43–45] Hence, ΔT decreases to be ∼50 K, which can be achieved by the sharp-edge contact [see Fig. 1(b)].

B. The roughness induced explosive boiling

A previous study investigated the effect of surface roughness on radiation heat transfer, showing that large scale roughness increases both the surface area for heat transfer and turbulent intensity compared to a smooth shiny surface.[46] The results indicate that the heat transfer can be increased by about 26% by using a saw-tooth rough surface than a smooth shiny one. Considering this roughness effect, the rough skirt ring increases radiation heat flux to raise the sunny side temperature of the droplet, enhancing the symmetry breaking between the sunny side and night side. This non-symmetry temperature is useful to produce thrust force for droplet propulsion.

In addition, the rough skirt ring provides sufficient bubble nucleation sites; hence, it functions as an *igniter*. When the heated droplet (fuel) contacts the skirt ring (igniter), explosive boiling is triggered. Based on the heterogeneous bubble nucleation theory, the active bubble nucleation sizes are in a range of $D_{c,min} \sim D_{c,max}$,[47]

$$D_{c\,max,\,min} = \frac{\delta_t \sin\beta}{2(1+\cos\beta)}\left(\frac{\Delta T_w}{\Delta T + \Delta T_{sub}}\right) \times \left[1 \pm \sqrt{1 - \frac{8\sigma T_{sat}(1+\cos\beta)(\Delta T_w + \Delta T_{sub})}{\Delta T^2 \delta_t h_{fg} \rho_v}}\right], \quad (1)$$

where δ_t, β, σ, T_{sat}, ρ_v, and h_{fg} are the thermal boundary layer thickness, the contact angle between solid and liquid, surface tension between vapor and liquid, saturation temperature, vapor density, and latent heat of evaporation, respectively. ΔT_{sub} is the liquid subcooling, which equals 0 for saturation boiling. ΔT_w is the wall superheating, equal to $T_r - T_{sat}$ in this study, where T_r is the skirt ring temperature. β got the measured value of $\beta = 55.6°$ for the water droplet on the rough skirt ring surface. Holding $\sigma = 0.0589$ N/m, $T_{sat} = 373.15$ K, $\rho_v = 0.598$ kg/m^3, and $h_{fg} = 2256.43$ kJ/kg for water–vapor system and wall superheating of $\Delta T_w = 91.4$ K for the skirt ring, D_c are (0.30–32.69) μm.

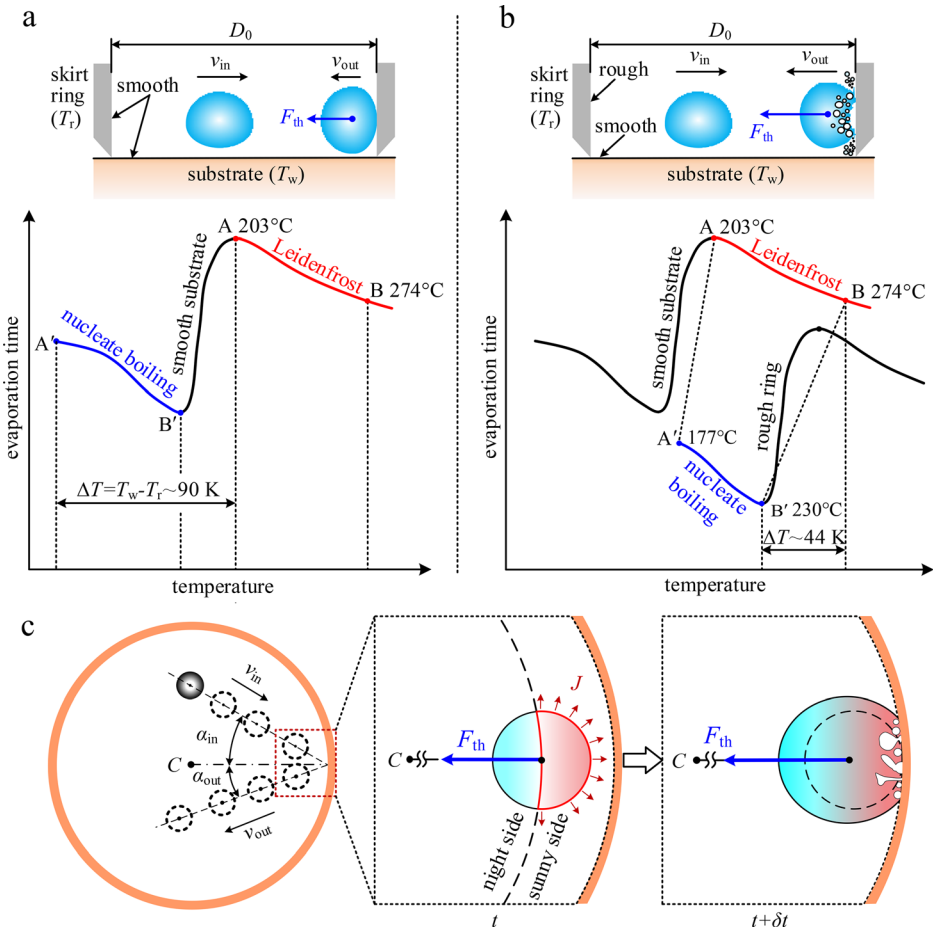

FIG. 1. Control of droplet dynamics by explosive boiling trigger. (a) Small thrust force produced via using both smooth surfaces of the substrate and skirt ring. (b) Sufficient thrust force via using the smooth substrate and rough skirt ring. (c) Thrust force produced due to the symmetry breaking of explosive boiling.

C. The explosive boiling induced propulsion force

Evaporation momentum force F_e is introduced to propel the droplet motion [see Fig. 1(c)]. Kandlikar indicates that F_e is caused by the non-symmetry evaporation around a bubble in a liquid under which momentum exchange results from mass transfer between liquid and vapor.[48,49] For a bubble growth on a heated wall, evaporation is stronger near the three-phase contact line of solid–liquid–vapor, adhering bubbles on the wall. The non-symmetry evaporation around the bubble delays bubble departure from the wall, relating to critical heat flux (*CHF*). Kandlikar proposed new *CHF* correlations incorporating the F_e effect.[48,49] Recently, the present authors investigated forced convective heat transfer of supercritical fluid in vertical tubes under heating conditions.[50,51] By analogizing to subcritical boiling, F_e is introduced to reflect the growth of vapor-like fluid layer δ_{vl} on the wall. The competition between F_e and inertia force (F_i) coming from the incoming fluid stream dominates the supercritical heat transfer.

For the present problem, when a Leidenfrost droplet approaches the skirt ring, the droplet can be divided into a sunny side and a night side [see Fig. 1(c)]. The rough skirt ring surface enhances radiation heat transfer toward droplet to elevate droplet temperature and evaporation rate on the sunny side than on the night side. When the droplet contacts with the skirt ring, skirt ring cavities trigger the contact boiling in the droplet. In the ~9.00 ms timescale, the explosive boiling yields fast droplet expansion due to miniature bubbles in the droplet, generating sufficient momentum exchange between the droplet and its surrounding gas (mixture of vapor and air) to achieve thrust force. This paper involves both the non-contact evaporation and contact boiling induce evaporation momentum force F_e, but the latter is seldom treated in the literature. The symmetry of evaporation and contact boiling is broken to generate thrust force.

Considering that a Leidenfrost droplet with an incoming velocity V_{in} and an incoming angle α_{in} approaches the skirt ring. After a collision with the wall, the reflection velocity and reflection angle become V_{out} and α_{out}, respectively. For droplet-wall collision, two limit conditions exist, referring to mirror reflection with $\alpha_{out}=\alpha_{in}$ and normal reflection with $\alpha_{out}=0$, reflectively. The practical collision is in between the two limit conditions. For sufficiently large thrust force, a line droplet trajectory can be achieved on the Leidenfrost surface. Traveling on the Leidenfrost surface and collision with the skirt ring in time-series creates droplet oscillation motion.

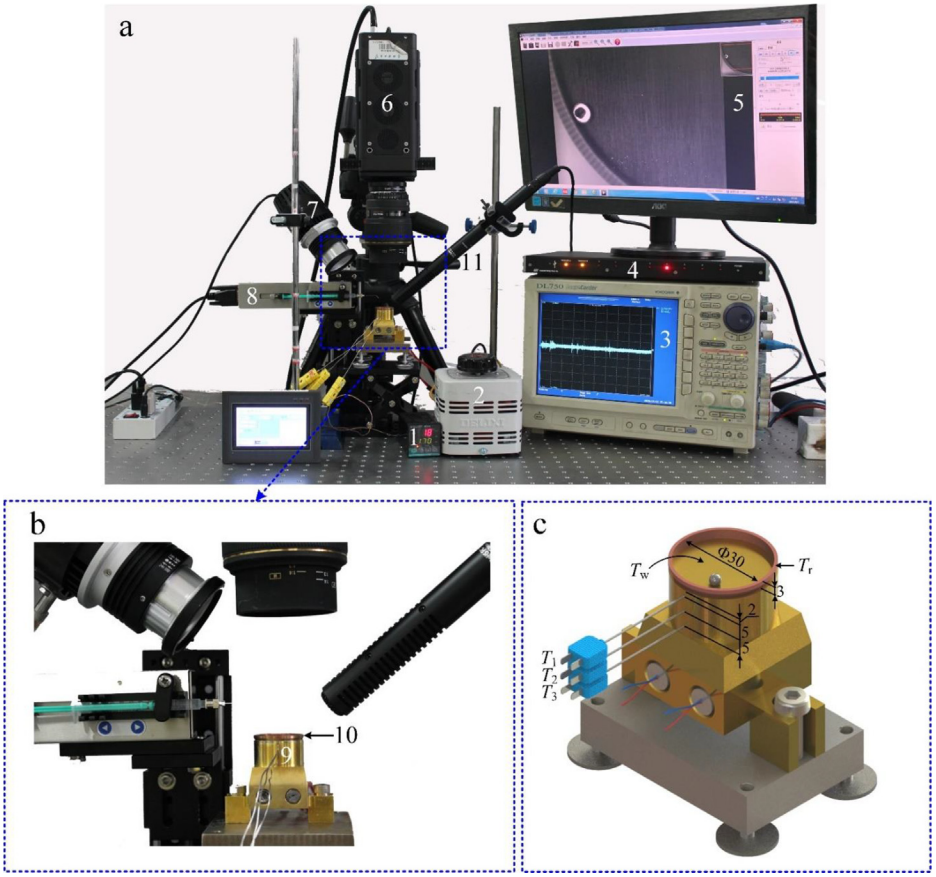

FIG. 2. Experiment setup (1: PID temperature controller; 2: voltage transformer; 3: high speed data acquisition system; 4: synchronizer; 5: PC screen; 6: high speed camera; 7: lamp; 8: micro-syringe pump; 9: brass substrate supporting the skirt ring; 10: copper skirt ring; and 11: microphone. All dimensions are in mm.) (a) The image of the experimental setup. (b) Focusing view of the test section. (c) Leidenfrost substrate having a sharp-edge contact with the skirt ring.

III. MATERIALS AND METHODS

A. Experimental setup

Figure 2 shows the experiment setup, including a brass substrate, a micro-pump for droplet emission, and measurement instruments. A power supply system provides heat to the system with a proportional integral derivative (PID) temperature controller. Three thermocouples are arranged in the height direction of the brass substrate. The substrate temperature T_w is obtained by extending the linear temperature distribution in the height direction to the surface location. The temperature is well controlled to be within 0.5 °C uncertainty. A micro-pump (RSP01-BDG) ejects a droplet, in which the droplet diameter is in the range of (2.6–2.8) mm. Initially, the droplet is ∼20 mm higher than the horizontal substrate plane. The instruments involve a high speed camera (MotionPro Y4, IDT, USA), a high speed Infrared Radiation image camera (InfrcTec, ImageIR 5380, USA), a microphone (SGC-578, China), a synchronizer (MotionPro Timing Hub, IDT, USA), and a high speed data acquisition system (DL750 ScopeCorder, YOKOGAWA, Japan). In this experiment, a water droplet is used with the physical properties shown in Table I.

B. Sample fabrication

The brass substrate has a cylinder shape. The top surface was polished with a 7000# sandpaper. Then, the top surface was treated by the polishing plate to form a mirror surface with a ∼20 nm roughness. The contact angle is 65.8°. The skirt ring has an internal diameter of 28 mm with a wall thickness of 1 mm. A sharp edge configuration is used to form the line contact with the brass substrate. Such a design ensures a suitable temperature difference between the substrate and skirt ring. The inner surface of the skirt ring was polished by the 80# sandpaper polishing technique to form a ∼1.65 μm roughness. The contact angle on the rough surface is 55.6°. For comparison purposes, a smooth skirt ring is made using a similar technique as for the substrate (Fig. S1 for the characterization of smooth surface and rough surface, including surface image files, 3D morphology, roughness distribution, and contact angles in the supplementary material).

C. Experimental methods

The measurement not only involves a long time duration covering the whole droplet lifetime in ∼1 min timescale but also involves a

TABLE I. Physical properties of water at atmospheric pressure.

Fluids	ρ_l kg/m^3	ρ_v kg/m^3	T_{sat} °C	h_{fg} kJ/kg	$\mu_v \times 10^4$ Pa s	λ_v W/(m K)	σ N/m
Water	1000	0.598	100	2256.4	2.821	0.6791	0.0589

short duration in (1–10) ms timescale. For long time measurement, the synchronizer coordinates the data acquisition of image files captured by a high-speed camera and sound voltage captured by the microphone. The synchro error is 20 ns to trigger different signals. The top view images were captured with the recording frequency of 250 fps with the spatial resolution of 34 μm. Thus, the droplet diameter has an uncertainty of 34 μm, which is 13% for the maximum error for the smallest D of 260 μm. To reduce the error for the traveling velocity of the droplet (V), two neighboring images are selected using the images file with the recording rate of 50 fps. The error of V depends on the magnitudes of V. The smallest V corresponds to a maximum error of 3.4%. To capture the droplet dynamics in the vertical plane with long time duration, the side view measurement using a high speed camera is also performed with the recording frequency of 500 fps.

Explosive boiling takes place very fast when colliding with the skirt ring. In order to capture the quick process, a separate measurement using a high speed camera was performed with a recording rate of 4000 fps. Thus, the time between two neighboring images is 0.25 ms under which the spatial resolution is 15.2 μm. Droplet surface temperatures were measured by a high-speed infrared radiation image camera with a spatial resolution of 11.9 μm and a temperature uncertainty of 0.4 °C. The major parameters, instruments, and uncertainties are summarized in Table S1 in the supplementary material.

IV. RESULTS AND DISCUSSION

A. Higher droplet temperatures and droplet deformation using a rough skirt ring

The substrate temperature T_w is kept to be higher than the Leidenfrost transition temperature T_t. During the collision of the droplet and skirt ring, explosive boiling is expected, by keeping the skirt ring temperature T_r lower than T_t. Thus, a suitable temperature difference between T_w and T_r shall be maintained. An easy method to achieve T_w–T_r is to use the sharp-edge contact between the skirt ring and substrate. The foot-print circular line contact between two pieces of materials creates a thermal resistance to achieve T_w–T_r. Before the formal experiment, a calibration experiment on T_w and T_r was performed in an air environment without involving droplet (see Fig. S2 in the supplementary material). T_r is self-adapted to the variation of T_w in a linear form, and T_w–T_r increases with the increase in T_w. Due to the significantly larger thermal inertia of the solid material than the droplet, the droplet dynamics control experiment did not alter the relationship between T_w and T_r compared to the calibration condition without involving droplet.

A practical coupling of $T_w = 223.0$ °C and $T_r = 191.4$ °C ensures perfect control of droplet dynamics by using a rough skirt ring. It is important to verify the effect of the skirt ring roughness on droplet temperatures. Comparative experiments were performed by using a rough skirt ring and a smooth skirt ring, respectively. Both experiments involved positing an initial ~2.8 mm diameter droplet on the Leidenfrost surface. The rough skirt ring sustains periodic droplet oscillation with line trajectories, but the smooth skirt ring sustains curved trajectories. Figure 3 shows the top view of the IR camera measured droplet temperatures (see Fig. S3 for temperature fields in the supplementary material). Because droplet evaporation is faster by using a rough skirt ring than by using a smooth skirt ring, the physical time to reach the same droplet diameter (smaller than the initial value) is different for both samples. For comparison purposes, the time is calibrated to be the same. The temperature response for rough and smooth skirt rings is different. Just before the collision of the droplet with the skirt ring for $D \sim 2$ mm, the approaching side attains temperatures of 130.8 °C for the rough skirt ring but 120.6 °C for the smooth skirt ring, respectively. It is interesting to note strong droplet deformation for the collision of the droplet and rough skirt ring, but weak deformation is identified when using a smooth skirt ring [see Fig. 3(a)] (Multimedia view). Similar features regarding higher temperature distribution and droplet deformation by using surface roughness are also found for other droplet sizes such as $D \sim 1.1$ mm [see Fig. 3(b)]. Qualitatively, the enhanced thermal behavior using a rough skirt ring is consistent with the finding regarding the surface roughness effect on heat transfer.[46]

Then, the droplet deformation during the collision of the droplet and rough surface is explained. A separate experiment was performed for droplet dynamics control using a droplet having the same initial size as used in Figs. 3(a) and 3(b). A synchronizer with a 20 ns synchronization time coordinates sound signal detection and a high-speed camera to capture top view images. The experiment was performed in a silent night environment for sound signal detection. For rough skirt rings, an apparent sound nose is detected during each collision in a ~7 ms timescale. Simultaneously, miniature bubbles are observed to be entrained in a droplet during each collision [see Fig. 3(c)] (Multimedia view). Our experiment verifies explosive boiling for the collision of the droplet and rough surface, resulting in droplet deformation. Thoroughly different outcomes are achieved by using a smooth (mirror) skirt ring. The droplet is not deformed except when it is exactly contacting with the skirt ring. Bubbles are never observed in droplet, indicating no contact boiling phenomenon. Because we focus on the runs with a rough skirt ring, the smooth skirt ring outcomes are not presented for temperatures.

B. Control outcomes of droplet dynamics using explosive boiling

Droplet motion is decoupled into the horizontal plane component and vertical direction component: mirror reflection with $\alpha_{in} = \alpha_{out}$ and normal reflection with $\alpha_{out} = 0$ (see Fig. 4). With the running condition exactly the same as that shown in Fig. 3, droplet dynamics is presented in Fig. 5, including droplet diameter D, collision frequency f, traveling velocity V (top view), and sound voltage. The droplet displays a perfect circular shape when traveling above the Leidenfrost surface, but it is deformed during a collision with the skirt ring. An equivalent droplet diameter is defined as $D = (D_x^2 D_y)^{1/3}$, where D_x and D_y are the two diameters in two perpendicular coordinates of x and y on the horizontal plane, assuming the elliptical shape of the droplet. f is $f = 1/\Delta t$, where Δt is the time difference between two neighboring collisions. V is calculated as $V = \Delta x/\delta t$, where Δx is the distance between two center mass locations of the droplet and δt is the time difference between the two consecutive images.

Following initial droplet depositing on the Leidenfrost surface, the droplet lifetime contains 184 times collisions with the skirt ring, corresponding to 184-line trajectories on the Leidenfrost surface. The whole droplet lifetime possesses decreased droplet size, increased collision frequency, increased traveling velocity, and decreased sound noise signal. These variation trends reflect the effect of the droplet size. Hence, three regimes are divided with

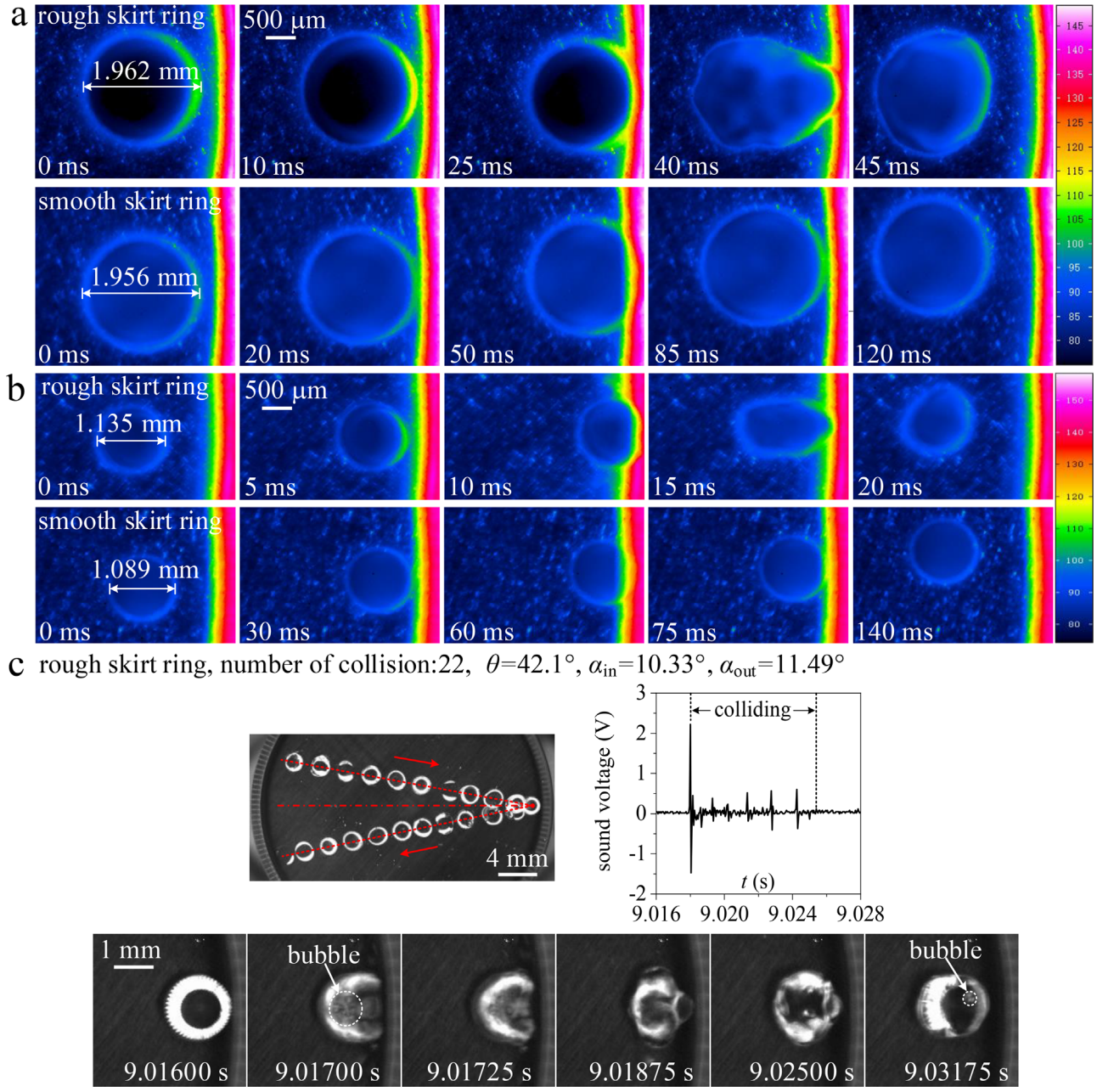

FIG. 3. Measured droplet temperatures, explosive boiling, and sound signal detection. (a) Infrared radiation images showing temperatures with the rough skirt ring and smooth skirt ring for $D \sim 2$ mm. (b) Temperature outcomes for $D \sim 1$ mm. (c) Line trajectories on the main heater surface, sound signal detection, and explosive boiling during a collision. Images are shown for the 22nd collision with $\alpha_{in} = 10.33°$ and $\alpha_{out} = 11.49°$, the sound signal at the impacting moment is up to 2.22 V, and miniature bubbles are observed in the droplet. Multimedia views: https://doi.org/10.1063/5.0091303.1; https://doi.org/10.1063/5.0091303.2; https://doi.org/10.1063/5.0091303.3

droplet diameters in the range of (1.35–2.79) mm in regime *I*, (0.50–1.35) mm in regime *II*, and (0–0.50) mm in regime *III*, respectively. f does not change too much and is ∼6 Hz in regime *I* but increases to (6.58–12.50) Hz in regime *II* and sharply increases to 27.78 Hz in regime *III*. Noting the logarithmic coordinate used in Fig. 5(c), V is (0.05–19.14) cm/s in regime *I* but increases to 39.42 cm/s in regime *II* and attains ∼85 cm/s in regime *III*. Droplet velocity is an important parameter for the control of droplet dynamics. Other techniques such as micrometer/millimeter sized saw-tooth structure attain the maximum speed of ∼38 cm/s.[36] The current work attains the maximum velocity, which is two times of that reported in the literature.

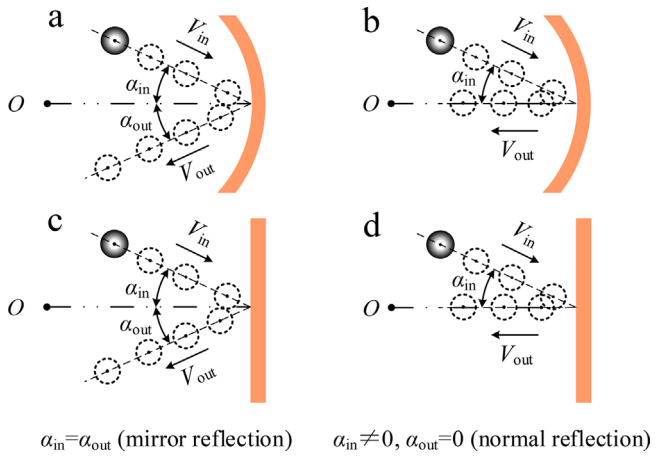

FIG. 4. Decoupling of droplet motion and collision. (a) and (b) are for top view. (c) and (d) are for side view.

Noise detection is widely applied in multiphase heat transfer to characterize boiling intensity.[52,53] The present experiment involves 184 pulses of sound noise corresponding to 184 times collisions with the skirt ring. In Fig. 5(d), the first noise signal refers to the collision with the Leidenfrost surface, but all the following pulse signals refer to the collisions with the skirt ring. In a large droplet size group, the explosive boiling induced noise attains sound voltages in the range of (0.13–2.82) V, which is stronger and can be apparently heard by human ears. The sound voltages decay in regimes *II* and *III*, indicating the explosive boiling intensity strongly dependent on droplet sizes.

Figure 6 shows sound voltages and instantaneous traveling velocities for specific runs of collision. A collision with a skirt ring weakly changes the direction of line trajectories before and after the collision. Figure 6(a) presents mirror reflection, but Figs. 6(b) and 6(c) presents normal reflection. Because normal reflection behaves line trajectory exactly passing through the Leidenfrost surface center, it is perfect for the control of droplet dynamics. The collision creates apparent acceleration. For example, V is 17.52 cm/s just before the 77th collision, drops to 5.47 cm/s during the collision, and sharply increases to 22.99 cm/s just after the departure from the skirt ring [see Fig. 6(b)]. After departure from the skirt ring, V displays a weak decrease due to the drag force of the droplet during its transport above the Leidenfrost surface. For an ideally uniform droplet explosion, V should be dropped to zero during a collision. However, explosive boiling yields strong droplet deformation in a ∼1 ms timescale, accounting for non-zero velocity during a collision. Two mechanisms account for droplet acceleration after collision. First, because droplet temperature is lower than the skirt ring, the contact between the droplet and skirt ring yields a temperature increase in the droplet. Second, explosive boiling in droplet converts a portion of thermal energy into kinetic energy. Figure 6 verifies the functions of enhanced heat transfer and bubble nucleation sites by using the rough surface of the skirt ring.

Figure 7 summarizes the droplet trajectories for all collisions during the whole droplet lifetime. Because a circular system is used, droplet trajectories almost cover the whole Leidenfrost surface for a large droplet size group [see Fig. 7(a)] (Multimedia view). An exact normal reflection with $\alpha_{out}=0$ ensures line trajectory passing through the circular surface center, but such an ideal condition is hardly encountered in experiments. Instead, we plot collections of the nearest location of line trajectories relative to the circular surface center, forming a focusing area (A_f), that is, significantly smaller than the Leidenfrost surface area (A_L). The ratios of A_f/A_L are 3.6%, 1.4% and 1.6% for the three droplet size groups, respectively [see Fig. 7(b)]. Even though the collision locations on the skirt ring are random, line trajectories pass through a very small focusing spot around the Leidenfrost surface center. The smaller ratios of A_f/A_L in medium and small droplet size groups indicate better control of trajectories with the decrease in droplet sizes, which will be explained later.

Because the nearest distance of a line trajectory relative to the Leidenfrost center depends on incoming and reflection angles, one is interested in the probability distributions of α_{in} and α_{out}, which have narrow distributions and they are overlapped with each other [see Fig. 7(c)]. For bigger droplet, quasi-flat distributions are within (14–20)% with α_{in} and α_{out} in the range of (0°–10°). For smaller droplet, the distribution becomes narrower, which accounts for ∼48% with the two angles in the range of (0°–2°). All the collisions in regimes *II* and *III* hold the two angles lower than 8° or 10°. Figure 7 concludes the mixed modes of mirror reflection and normal reflection for D in the range of (2.79–1.35) mm, but normal reflection dominates for $D<1.35$ mm.

Trajectories present quasi-uniform distribution in regime *I* but switch to fan shape distribution covering a circumferential angle $\Delta\theta$ of 121.3° in regime *II* and a slim rectangular distribution in regime *III* [see Fig. 7(a)]. Trajectories distribution is dependent on the relative importance of thrust force (F_{th}), inertia force (F_i), and gravity force (F_g). Later, we will show that F_{th} obeys the $\sim D^2$ law, but F_i and F_g obey the $\sim D^3$ law, yielding the scaling law of $F_{th}/F_i \sim D^{-1}$ and $F_{th}/F_g \sim D^{-1}$. Because F_{th} prefers the droplet passing through the Leidenfrost surface center (normal reflection), the D^{-1} scale law ensures the switch from mirror reflection to normal reflection for smaller droplet, explaining smaller α_{in} and α_{out} and narrowed range of the two angels for smaller droplet [see Fig. 7(c)]. The D^{-1} scale law also explains the narrowed fan distribution of line trajectories for smaller droplet [see Fig. 7(a)] under which the droplet sustains the pulsating flow driven by consecutive collisions between two opposite side locations of the skirt ring.

For a Leidenfrost droplet floating on a hot plate, jumping hardly occurs.[54] Jumping may only occur in the final stage of the Leidenfrost phenomenon under which the vapor layer underneath the droplet is broken for small droplet (∼19 μm for water).[54] One remembers that once a droplet collides with the sidewall of the skirt ring, thrust force should have a vertical component, enhancing the transport capability in the air. Separate time-series images are taken for side view. Striking of a ∼0.86 mm droplet on the skirt ring triggers a long-distance transport in the air with parabola trajectory, followed by consecutive collisions of the droplet with the Leidenfrost surface and skirt ring [see Fig. 8(a)] (Multimedia view). The parabolic transport in the air and jumping on the Leidenfrost surface result in smaller drag force, partially explaining larger traveling velocities than those without jumping.

When using a smooth skirt ring, side and top view visualization results are presented in Figs. 8(b) (Multimedia view) and 9 (Multimedia view), respectively. Line trajectory (top view) does not exist at all (see Fig. 9). The whole droplet lifetime is still divided into three sub-stages. In a large size group, after a collision with the skirt ring, the droplet travels as a curved trajectory and reaches another location of the skirt ring, not the opposite location of the skirt ring

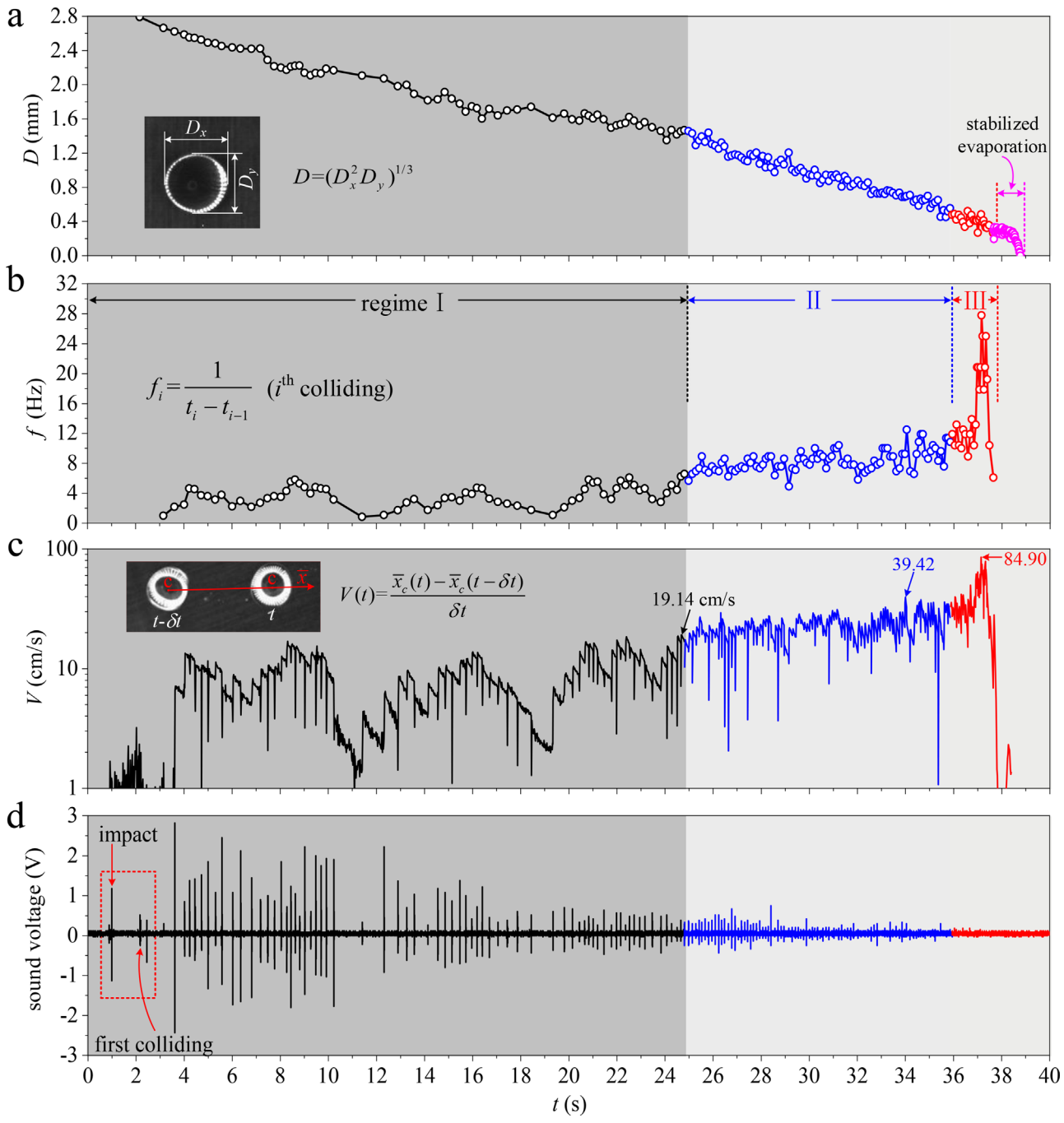

FIG. 5. Droplet dynamics with $T_w = 223.0\,^{\circ}\text{C}$ and $T_r = 191.4\,^{\circ}\text{C}$. (a) $D \sim t$. (b) $f \sim t$. (c) $V \sim t$. (d) sound voltage $\sim t$.

with respect to the previous collision, under which the thrust force is caused by non-symmetry evaporation, not by explosive boiling. The curved trajectory infers the competition of thrust force with inertia force and gravity force to dominate droplet motion. When droplet sizes are changed to be smaller than ~1.69 mm, collisions with the skirt ring are very weak. Droplet trajectories display the extended *surface roughness* feature along the sidewall of the skirt ring. Marangoni effect sticks the droplet around the sidewall of the skirt ring. The Leidenfrost substrate has large thermal inertia to keep constant and uniform temperature. Due to the sharp-edge contact between the skirt ring and the substrate, the lower temperature of the skirt ring *attracts* the droplet due to the Marangoni effect. In fact, the

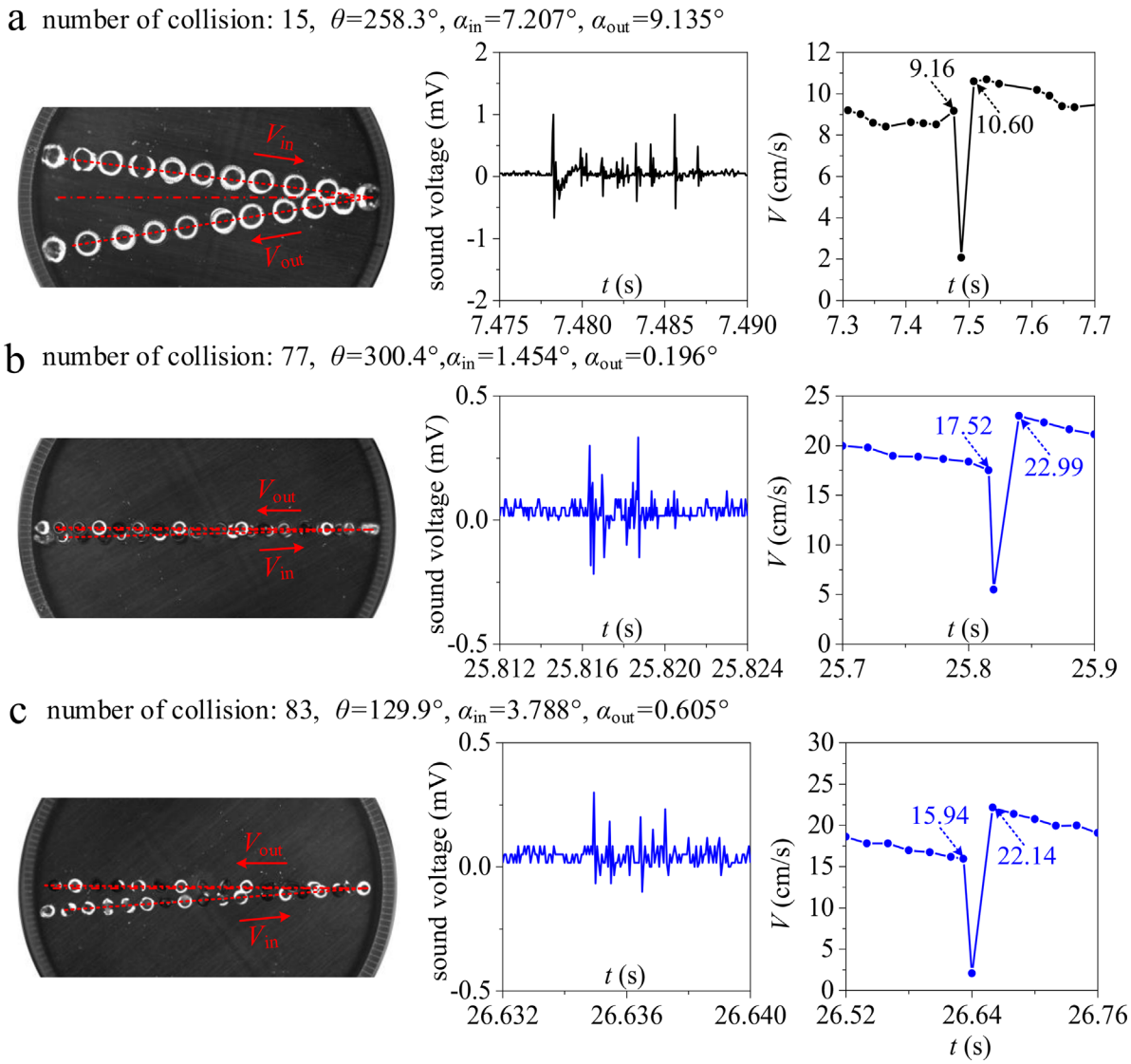

FIG. 6. Droplet trajectories, sound voltage during a collision, and velocities before and after the collision. (a) Collision number of 15. (b) Collision number of 77. (c) Collision number of 83. (d) Collision number of 83.

Marangoni effect also exists for the rough skirt ring case, but the Marangoni force is thoroughly suppressed by the thrust force. The droplet cannot be stuck near the skirt ring, instead, a large thrust force during collision ejects the droplet just like a bullet. In summary, we indicate the effectiveness of a rough skirt to trigger explosive boiling, supplying sufficient thrust force to manipulate the droplet motion.

The two-surface temperatures are the parameters to control the droplet motion. For such purposes, T_w has the range of (203–274) °C, corresponding to T_r in the range of (177–230) °C. Figures 5–8 show the control outcomes with $T_w = 223.0$ °C and $T_r = 191.4$ °C. To demonstrate the repeatable experiment, another run with $T_w = 232.5$ °C and $T_r = 200.1$ °C is shown in Fig. 10, in which Figs. 10(a)–10(c) demonstrate line trajectories, focusing spot and distribution of incoming and reflection angles. It is seen that the control outcomes shown in Fig. 10 are very similar to those shown in Fig. 7, even though the two runs had different temperatures of the substrate and skirt ring.

C. Scaling law analysis for the control of droplet dynamics

Thrust force (F_{th}), inertia force (F_i), gravity force (F_g), and drag force (F_d) are competed to influence droplet dynamics. F_{th} is[55]

$$F_{th} = \frac{d(mv)}{dt} = v\frac{dm}{dt} + m\frac{dv}{dt}, \tag{2}$$

where m, v, and t are the droplet mass, expansion velocity due to non-symmetry phase change, and time, respectively. mv is the droplet momentum. The following equations exist:

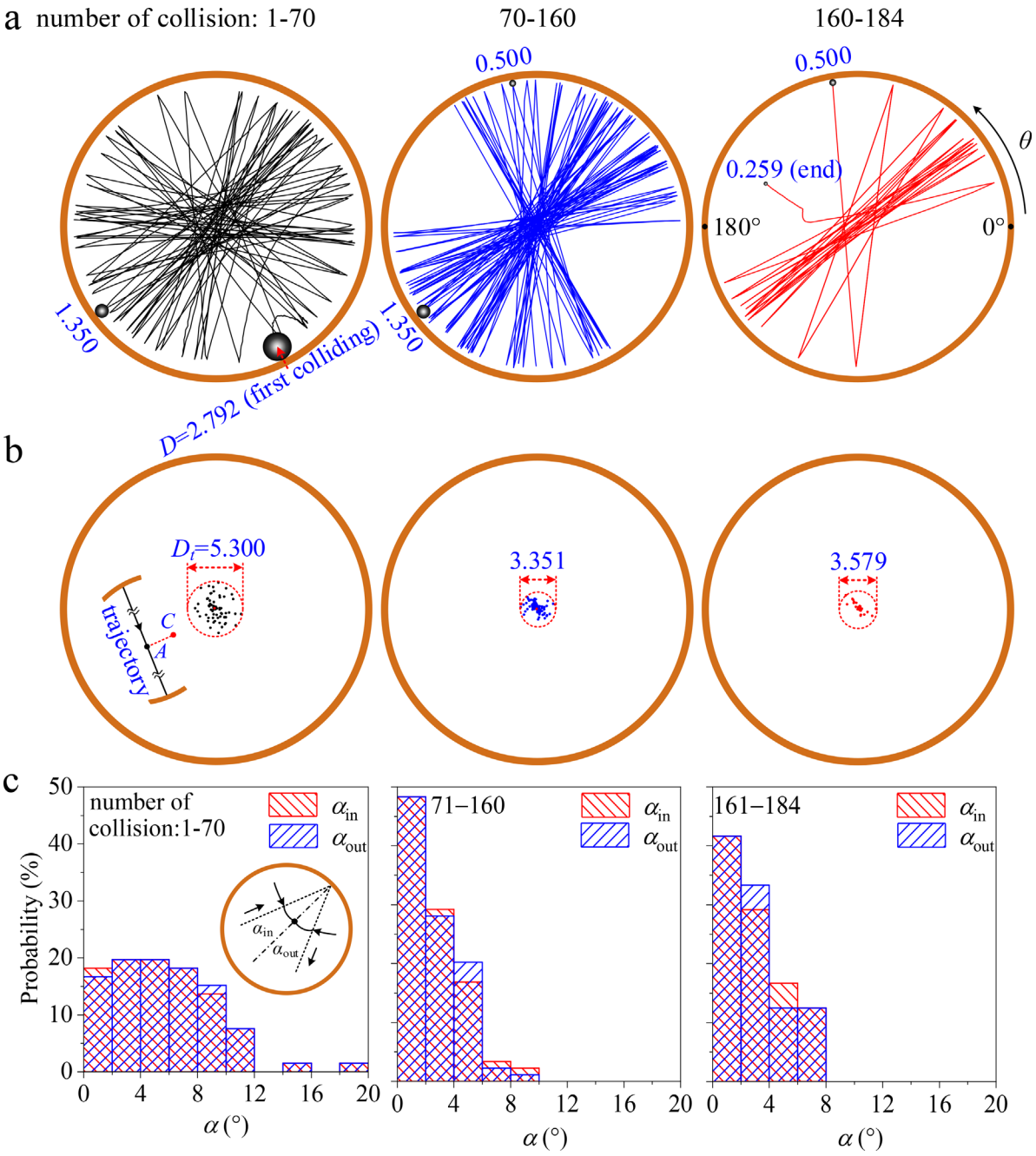

FIG. 7. The control of droplet motion. (a) Line trajectories in three regimes of droplet diameters. (b) Focusing area around the main heater surface center. (c) Probability distributions of incoming and reflection angles. Multimedia view: https://doi.org/10.1063/5.0091303.4

$$v = \frac{1}{2}\frac{\mathrm{d}D}{\mathrm{d}t}, \quad \frac{dv}{dt} = \frac{1}{2}\frac{\mathrm{d}^2D}{\mathrm{d}t^2}. \tag{3}$$

We consider a droplet contacting with the skirt ring with a contact angle of β. The heat flux due to wall heating is q. The mass conservation yields[55]

$$m = \frac{\pi}{24}\rho_l D^3\left(2 + 3\cos\beta - \cos^3\beta\right). \tag{4}$$

Hence, we have

$$\frac{\mathrm{d}m}{\mathrm{d}t} = \frac{\pi\rho_l D^2}{8}\frac{\mathrm{d}D}{\mathrm{d}t}\left(2 + 3\cos\beta - \cos^3\beta\right). \tag{5}$$

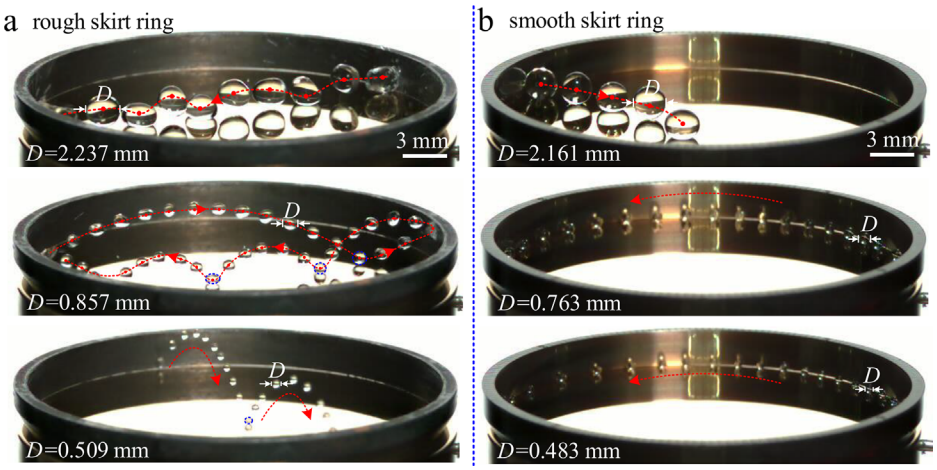

FIG. 8. Side view of droplet trajectories for different droplet sizes. (a) Rough skirt ring outcomes. (b) Smooth skirt ring outcomes. Multimedia views: https://doi.org/10.1063/5.0091303.5; https://doi.org/10.1063/5.0091303.6

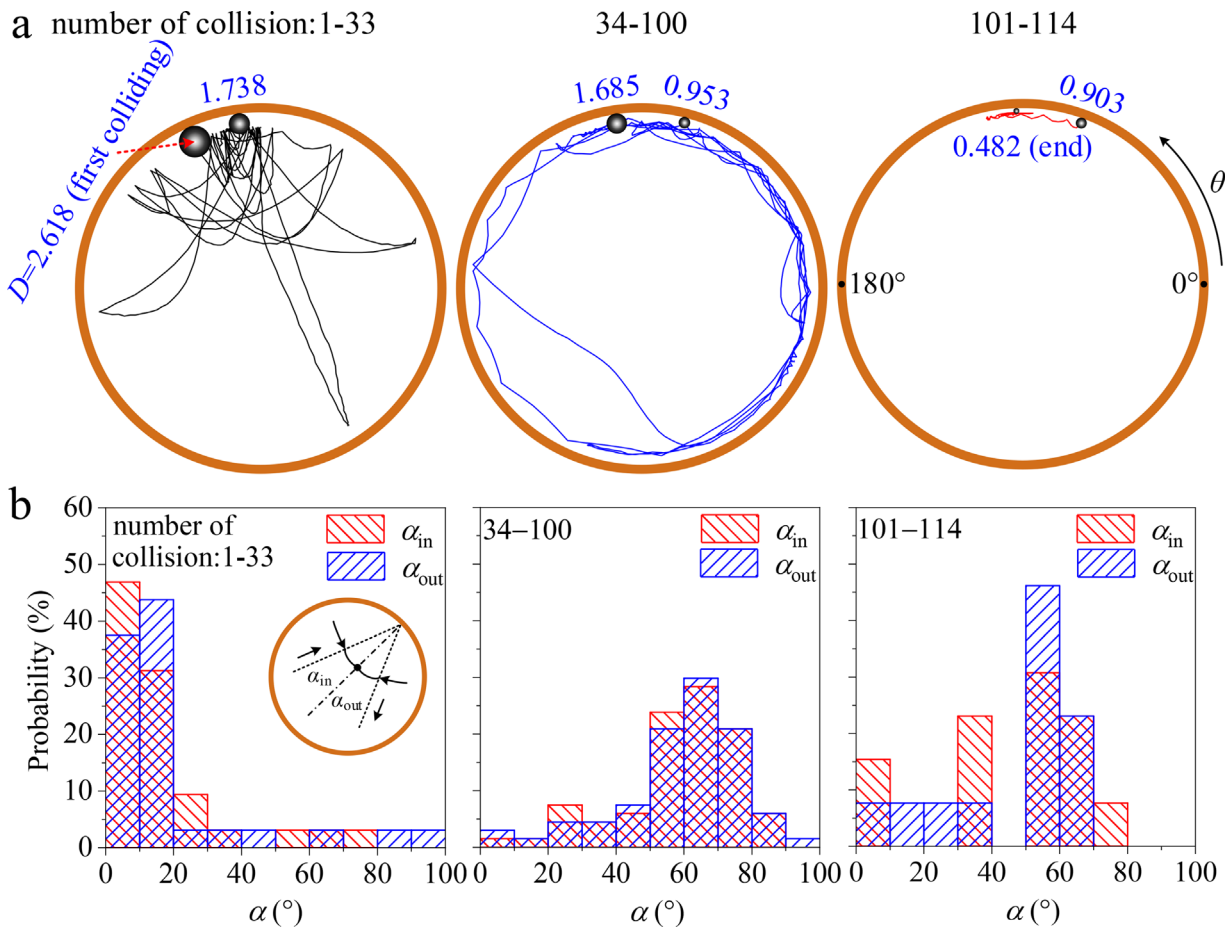

FIG. 9. Droplet motion via using a smooth skirt ring. (a) Curved trajectories in terms of three regimes of droplet diameters. (b) Scattered distribution of incoming and reflection angles. Multimedia view: https://doi.org/10.1063/5.0091303.7

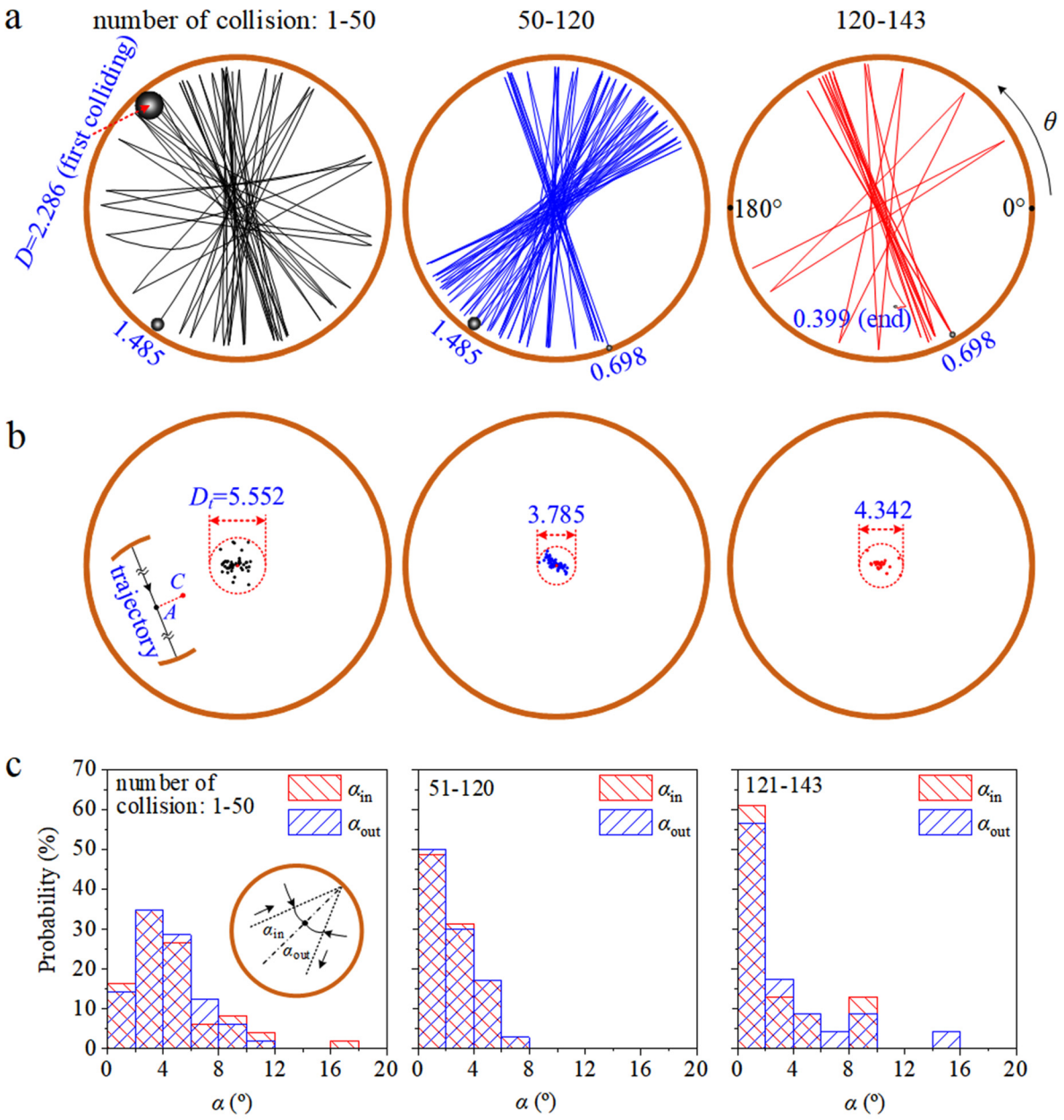

FIG. 10. The control of droplet motion with $T_w = 232.5\,^{\circ}\mathrm{C}$ and $T_r = 200.1\,^{\circ}\mathrm{C}$. (a) Line trajectories in three regimes of droplet diameters. (b) Focusing area around the main heater surface center. (c) Probability distributions of incoming and reflection angles.

Based on the energy conservation, the mass change rate is

$$\frac{\mathrm{d}m}{\mathrm{d}t} = \frac{q \cdot \pi(\mathrm{D}\sin\beta)^2}{4h_{\mathrm{fg}}}, \tag{6}$$

where h_{fg} is the latent heat of evaporation. Combining Eqs. (5) and (6) yields

$$\frac{\mathrm{d}D}{\mathrm{d}t} = \frac{2q\sin\beta^2}{\rho_l h_{\mathrm{fg}}(2 + 3\cos\beta - \cos^3\beta)}. \tag{7}$$

Substituting Eqs. (3), (4), (5), and (7) into Eq. (2) yields

$$F_{\mathrm{th}} = \frac{\pi D^2 q^2 \sin^4\beta}{4\rho_l h_{\mathrm{fg}}^2(2 + 3\cos\beta - \cos^3\beta)} \sim D^2. \tag{8}$$

A spheric droplet has the inertia force and gravity force expressed as

$$F_i = \frac{\pi\rho_l D^3}{6}\frac{dV}{dt} \sim D^3, \quad F_g = \frac{\pi\rho_l D^3}{6} g \sim D^3, \tag{9}$$

where V is the traveling velocity, not the expansion velocity v, and g is the acceleration of gravity.

Drag force F_d for a droplet in the air is written as[56]

$$F_d = \frac{1}{8}\rho_{air}(V_{air} - V)^2 \pi D^2 C_d, \tag{10}$$

where ρ_{air} and V_{air} are the air density and velocity, $V_{air} = 0$ in stationary air, and C_d is the drag coefficient. For the laminar flow of droplets in the air, C_d is[56]

$$C_d = \frac{24}{\mathrm{Re}}, \quad \mathrm{Re} = \frac{\rho_l (V - V_{air}) D}{\mu_{air}}, \tag{11}$$

where μ_{air} is the viscosity of air. Substituting Eq. (11) into Eq. (10) yields

$$F_d = 3\pi \mu_{air} V D \sim D. \tag{12}$$

Hence, Eqs. (8), (9), and (12) yield the relative importance of the above forces as follows:

$$\frac{F_{th}}{F_i} \sim D^{-1}, \quad \frac{F_{th}}{F_g} \sim D^{-1}, \quad \frac{F_{th}}{F_d} \sim D. \tag{13}$$

We note that Eqs. (10) and (11) are the drag force for drop motion surrounding air. For Leidenfrost droplet motion traveling above a vapor film, the viscous drag force F_μ can be predicted as[57]

$$F_\mu = (\mu_v V/\varepsilon) l^2, \quad l \approx R^2 \kappa, \quad \kappa = \sqrt{\frac{\rho_l g}{\sigma}}. \tag{14}$$

The vapor layer thickness ε is predicted as[58]

$$\varepsilon = \left[\frac{3\lambda_v \Delta T_{sat} \rho_l \mu_v g}{4 h_{fg} \rho_v \sigma^2}\right]^{1/4} R^{5/4}. \tag{15}$$

In Eqs. (14) and (15), μ_v is the vapor viscosity, V is the droplet velocity, l is the characteristic length, R is the drop radius, λ_v is the thermal conductivity of vapor, ΔT_{sat} is the wall superheating, and h_{fg} is the latent heat of evaporation.

For an elastic collision between a body and a wall without energy dissipation, mirror reflection dominates with $\alpha_{in} = \alpha_{out}$ and $V_{in} = V_{out}$. For the present problem, the inertia force of the droplet tends to satisfy mirror reflection, deviating the trajectory from the Leidenfrost surface center. Gravity force tends to populate a droplet in a lower position. Drag force tends to slow down a droplet motion. The thrust source is only the driving force tending to regulate the droplet trajectory passing through the Leidenfrost surface center. Hence, the ratios of F_{th}/F_i and F_{th}/F_g govern the droplet dynamics.

F_{th}, F_i, and F_d are calculated based on Eqs. (8), (9), and (12), respectively. In Eq. (8), a key parameter is the heat flux during explosive boiling in the ~9.00 ms timescale. For violent boiling, it is difficult to accurately determine q. It is reported that q reaches 18.5 MW/m^2 for ultra-high heat flux boiling.[59] Corresponding to the wall superheating,[59] the boiling heat transfer coefficient reaches 308 kW/m^2 K. Integrating this heat transfer coefficient with the wall superheating of $T_r - T_{sat} = 464.5 - 373.1 = 91.4$ K in the present study, q is estimated as 28.18 MW/m^2 to be used here. In Eqs. (9) and (12), V and dV/dt are the traveling velocity and acceleration, which are determined based on the measurement outcomes in Fig. 5(c). Having F_{th}, F_i, and F_d, one can achieve the scaling law expressed in Eq. (13).

F_{th}/F_d and F_{th}/F_μ vs D are shown in Fig. 11 with the black curve using Eqs. (10) and (11) for drag force F_d surrounding by air and the blue curve using Eqs. (14) and (15) for viscous drag force F_μ above a vapor film. The two curves are intercrossed with each other at D ~ 1.3 mm, and the drag forces using different calculations are in the same magnitude. For both curves, most of the data points are larger than 1, demonstrating larger F_{th} than F_d or F_μ. Figure 11 concludes the dominant force of F_{th} (the thrust force, or say, the evaporation momentum force). For smaller droplet in the later stage of the process, F_{th}/F_d or F_{th}/F_μ can be smaller than 1, explaining the stopped motion for fine droplet such as ~100 μm. Figure 11 verifies the scaling law of $F_{th}/F_d \sim D$.

In the present study, Eq. (13) presents the thrust force relative to other forces obeying the D^{-1} or D law. Here, we use such a scaling law to explain our experimental observations. Recall that Figs. 5 and 7 are plotted for droplet dynamics vs time over the entire droplet lifetime by subdividing the time into three regimes. These three regimes correspond to three drop size ranges. The general trend shown in Figs. 5 and 7 clearly shows that the droplet traveling velocity V increases with a decrease in droplet diameter D, and the distribution of incoming and reflecting angles becomes more narrowed when D decreases. Replot these results in Fig. 12 for V, α_{in}, α_{out}, and δ/D_0 vs D^{-1}. The scaling laws of $F_{th}/F_i \sim D^{-1}$ and $F_{th}/F_g \sim D^{-1}$ indicate that the contribution of thrust force to the droplet dynamics becomes more dominant when D decreases. V should be larger for the increased contribution of thrust force relative to other forces, explaining the increased V vs D^{-1} [see Fig. 12(a)]. The scaling law of thrust force relative to other forces also influences the distribution of α_{in} and α_{out}. The larger contribution of thrust force relative to other forces explains smaller α_{in} and α_{out} as well as the smaller deviation of line trajectories from the plate center point when D^{-1} increases, or say, at smaller drop sizes

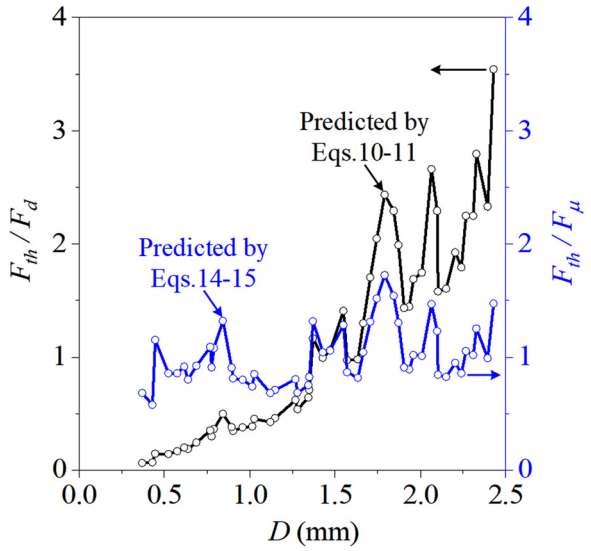

FIG. 11. The calculated results of F_{th}/F_d and F_{th}/F_μ dependent on D.

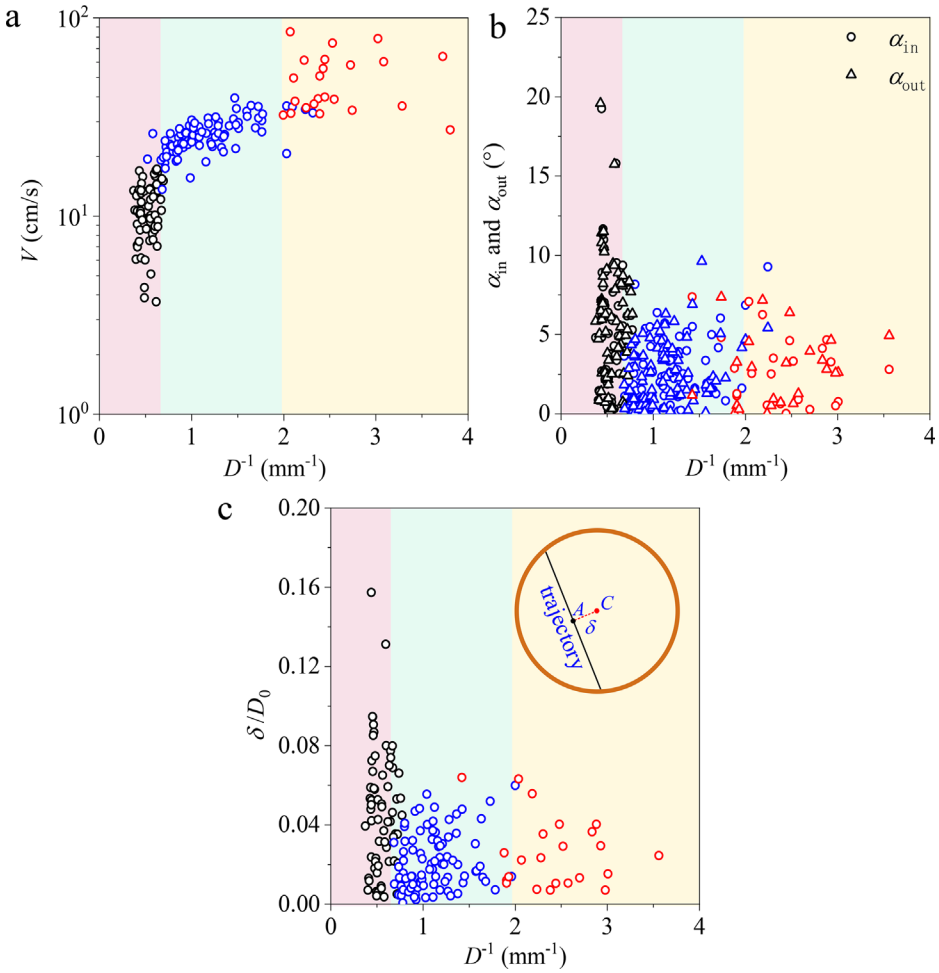

FIG. 12. The measured results satisfying the scaling law analysis. (a) $V \sim D^{-1}$. (b) α_{in} and α_{out} vs D^{-1}. (c) δ/D_0 vs D^{-1}.

[see Figs. 12(b) and 12(c)]. Figure 12 does not represent the scaling law itself but explains the control outcomes using the D^{-1} scale law.

D. Comments on the dominant mechanism for droplet control

A novel working principle is proposed to control droplet motion, which is fulfilled via the mixed mode of Leidenfrost on the main heater surface and nucleate boiling on a sharp-edged contact surface. The main heater surface is smooth and maintains a higher temperature than the skirt ring. The skirt ring roughness ($\sim\mu$m scale) triggers explosive boiling to create sufficient thrust force, ensuring a droplet to have line trajectories with high speed and to pass through the main heater surface center with a small focusing area. The evaporation momentum force is the dominant mechanism.

To further verify this dominant mechanism, the comparative experiment was performed with both smooth surfaces of the main heater and the skirt ring. Under such circumstances, the evaporation momentum force is weak, due to the weak heat transfer between the droplet and skirt ring. Thus, for the droplet curved trajectories, there is no focusing area at all (see Fig. 9).

Several groups identified droplet rotating motion.[57,60,61] Bouillant *et al.*[57] reported that Leidenfrost droplet initially at rest on horizontal substrates self-rotate and self-propel in the direction that they are rolling in the absence of any source of asymmetry or external force. The droplet rotating is found to be influenced by drop sizes. For large drops such as $R \sim 1.5$ mm, two convective cells are identified in the droplet, causing symmetry flow without bulk droplet rotating [see Fig. 13(a)]. However, when drop size decreases to $R < 1.5$ mm, a single convective cell is observed in the droplet, under which the flow symmetry is broken to yield bulk droplet rotating [see Fig. 13(b)]. The rapid internal flow accompanies by a tilting of their base, which creates a permanent ratchet-like mechanism, entraining the rolling liquid despite the fact that it is not in contact with its substrate [see Fig. 13(c)]. In our experiment, droplets may also rotate occasionally, which is observed by tracking a bubble in the droplet. Figure 14 shows a typical case with $T_w = 223.0\,^{\circ}$C and $T_r = 191.4\,^{\circ}$C. The droplet moves to the left [see Fig. 14(a)]. After the 26th collision with the skirt ring, the droplet moves to the right [see Fig. 14(b)].

Our experiment indicates that after each collision with the sidewall of the skirt ring, the reflection angle α_{out} is not exactly the same as the incoming angle α_{in} [see Fig. 7(c)]. The deviation of α_{out} from α_{in}

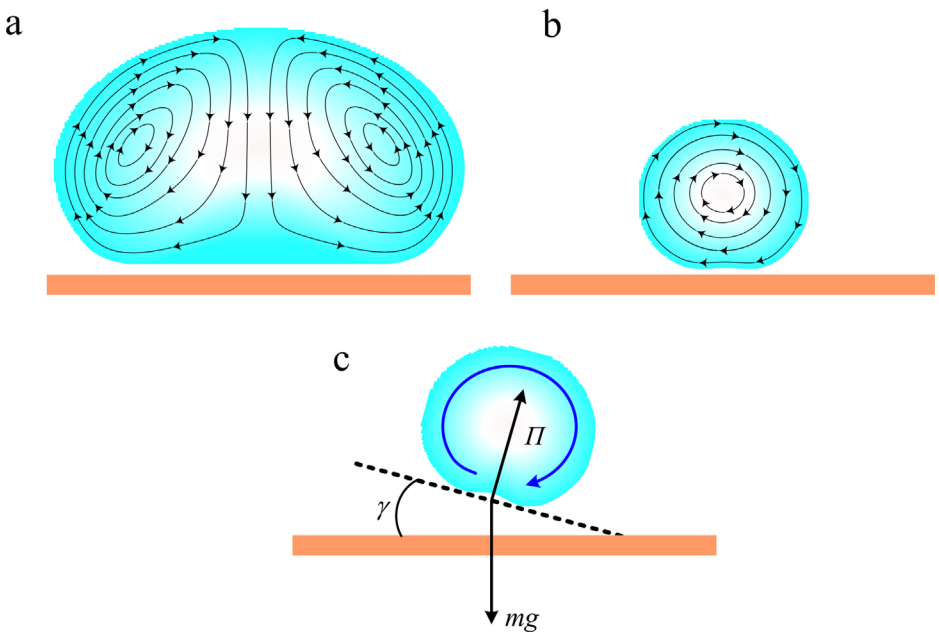

FIG. 13. Leidenfrost droplet rotating. (a) Large droplet rotating with two internal convective cells. (b) Symmetry breaking with a single convective cell. (c) Drop levitating is titled on average by an angle γ. This figure is replotted based on Ref. 57.

can be partially explained by the droplet rotating motion. Considering that a solid ball is approaching an elastic wall with its incoming angle of α_{in}. If the ball does not rotate, the reflection angle α_{out} should be the same as α_{in}. However, if the ball rotates in the anticlockwise direction, the reflection angle is smaller than the incoming angle [see Fig. 15(a)]. Otherwise, the reflection angle becomes to be larger than the incoming angle [see Fig. 15(b)]. During the collision of a body with a wall, a friction force is generated to alter the reflection angle. For the present problem, an example is given for Fig. 14, in which $\alpha_{out} = 1.06^{\circ}$, which slightly deviates from $\alpha_{in} = 1.72^{\circ}$. In summary, the dominant contribution of the thrust force causes the control of droplet motion in line trajectories and passing through the plate center within a small focusing spot. The droplet rotating motion partially explains the small deviation of the reflection angle from an incoming angle.

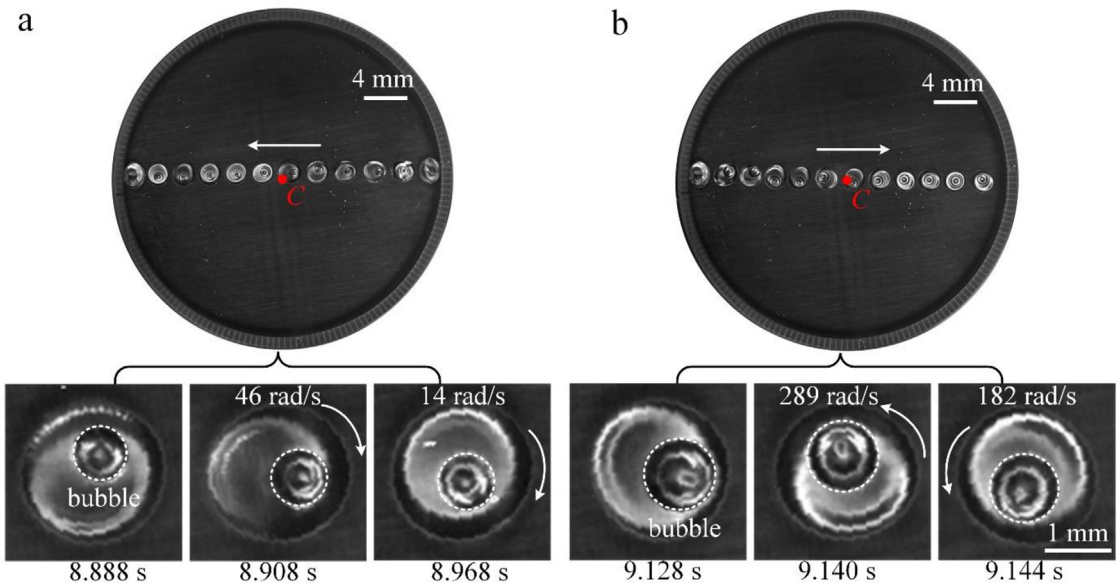

FIG. 14. The rotating of droplet does not influence line trajectories passing through the main heater center. (a) Droplet traveling to left. (b) Droplet traveling to right after collision with the skirt ring.

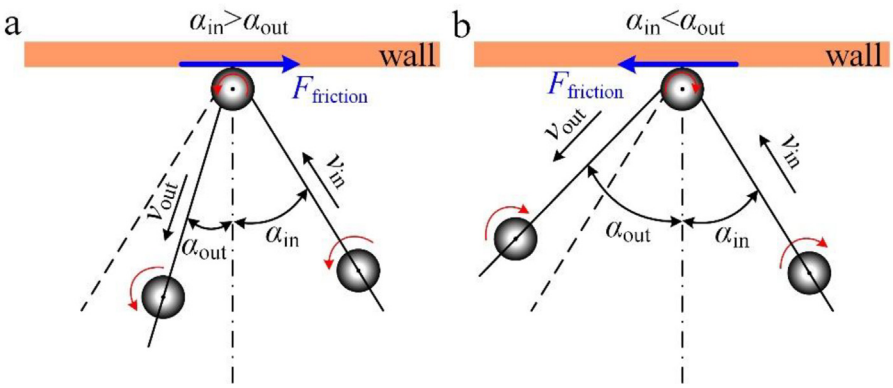

FIG. 15. Effect of rotating motion on the deviation of reflection angle from an incoming angle. (a) The reflection angle is smaller than the incoming angle when the ball rotates in an anticlockwise direction. (b) The reflection angle is larger than the incoming angle when the ball rotates in a clockwise direction. This figure is replotted based on Ref. 62.

V. CONCLUSIONS

A Leidenfrost droplet has ultra-low resistance for transportation. Previous studies used micro/nanostructures fabricated on a hot surface such as saw-tooth structure,[22,23,26] wettability gradient,[27–29] and structure gradient.[25,27,29] These structures create an imbalance force for droplet motion. Here, we introduce another material having a lower temperature than the main heater surface. The main heater surface works in the Leidenfrost mode, but the skirt ring works in the nucleated boiling mode. The sandpaper polishing technique is simple but effective for the preparation of the two kinds of surfaces. The $\sim\mu$m scale roughness on the skirt ring surface not only enhances radiation heat transfer but also supplies sufficient nucleation sites to trigger explosive boiling to emit a droplet. The thrust force is large enough to overcome inertia force and drag force, generating a line trajectory to reach a target location. This principle converts random motion to line motion for droplets. In our experiment, for all the collisions between the droplet and skirt ring, the droplet displays line motion to pass through a focusing area that is ~1% of the Leidenfrost surface area. The traveling velocity attains ~85 cm/s, larger than the value reported in the literature.

After performing the following studies: (1) well controlled droplet motion via the rough skirt ring, (2) not controlled droplet motion via the smooth skirt ring, (3) scaling law analysis, and (4) the effect of droplet rotating on the control of droplet dynamics, we conclude the dominant mechanism of evaporation momentum force produced via rough surface induced explosive boiling.

SUPPLEMENTARY MATERIAL

See the supplementary material for the details of the experimental information.

ACKNOWLEDGMENTS

The authors acknowledge support from the Beijing Nature Science Foundation (Grant No. 3222045), the National Nature Science Foundation of China (No. 52130608), and the Key Laboratories for National Defense Science and Technology (No. 6142702200510).

AUTHOR DECLARATIONS

Conflict of Interest

The authors have no conflicts to disclose.

DATA AVAILABILITY

The data that support the findings of this study are available from the corresponding author upon reasonable request.

REFERENCES

[1]J. G. Leidenfrost, "On the fixation of water in diverse fire," Int. J. Heat Mass Transfer **9**(11), 1153–1166 (1966).
[2]C. Liu, J. Sun, Y. Zhuang, J. Wei, J. Li, L. Dong, D. Yan, A. Hu, X. Zhou, and Z. Wang, "Self-propelled droplet-based electricity generation," Nanoscale **10**(48), 23164–23169 (2018).
[3]I. U. Vakarelski, J. O. Marston, D. Y. Chan, and S. T. Thoroddsen, "Drag reduction by Leidenfrost vapor layers," Phys. Rev. Lett. **106**(21), 214501 (2011).
[4]D. A. Lavan, T. McGuire, and R. Langer, "Small-scale systems for in vivo drug delivery," Nat. Biotechnol. **21**(10), 1184–1191 (2003).
[5]J. R. Baylis, J. H. Yeon, M. H. Thomson, A. Kazerooni, X. Wang, A. E. S. John, E. B. Lim, D. Chien, A. Lee, and J. Q. Zhang, "Self-propelled particles that transport cargo through flowing blood and halt hemorrhage," Sci. Adv. **1**(9), e1500379 (2015).
[6]A. A. Darhuber and S. M. Troian, "Principles of microfluidic actuation by modulation of surface stresses," Annu. Rev. Fluid Mech. **37**, 425–455 (2005).
[7]Y. Lin, Z. Hu, M. Zhang, T. Xu, S. Feng, L. Jiang, and Y. Zheng, "Magnetically induced low adhesive direction of nano/micropillar arrays for microdroplet transport," Adv. Funct. Mater. **28**(49), 1800163 (2018).
[8]X. Yu, Y. Zhang, R. Hu, and X. Luo, "Water droplet bouncing dynamics," Nano Energy **81**, 105647 (2021).
[9]J. Yang, L. C. Chow, and M. R. Pais, "Nucleate boiling heat transfer in spray cooling," J. Heat Transfer **118**(3), 668–668 (1996).
[10]Z. Zhang, R. Zhou, X. Ge, J. Zhang, and X. Wu, "Perspectives for 700 °C ultra-supercritical power generation: Thermal safety of high-temperature heating surfaces," Energy **190**, 116411 (2020).
[11]S. Adera, R. Raj, R. Enright, and E. N. Wang, "Non-wetting droplets on hot superhydrophilic surfaces," Nat. Commun. **4**, 2518 (2013).
[12]C. Kruse, T. Anderson, C. Wilson, C. Zuhlke, D. Alexander, G. Gogos, and S. Ndao, "Extraordinary shifts of the Leidenfrost temperature from multiscale micro/nanostructured surfaces," Langmuir **29**(31), 9798–9806 (2013).
[13]H. Kwon, J. Bird, and K. Varanasi, "Increasing Leidenfrost point using micro-nano hierarchical surface structures," Appl. Phys. Lett. **103**, 201601 (2013).
[14]M. Shi, R. Das, S. Arunachalam, and H. Mishra, "Suppression of Leidenfrost effect on superhydrophobic surfaces," Phys. Fluids **33**, 122104 (2021).
[15]B. Ng, Y. Hung, and M. Tan, "Suppression of the Leidenfrost effect via low-frequency vibrations," Soft Matter **11**(4), 775–784 (2015).
[16]A. Shahriari, J. Wurz, and V. Bahadur, "Heat transfer enhancement accompanying Leidenfrost state suppression at ultrahigh temperatures," Langmuir **30**(40), 12074–12081 (2014).
[17]I. Tiginyanu, T. Braniste, D. Smazna, M. Deng, F. Schütt, A. Schuchardt, M. A. Stevens-Kalceff, S. Raevschi, U. Schürmann, L. Kienle, N. M. Pugno, Y. K.

Mishra, and R. Adelung, "Self-organized and self-propelled aero-GaN with dual hydrophilic-hydrophobic behaviour," Nano Energy **56**, 759–769 (2019).
[18]X. Sun, Y. Feng, B. Wang, Y. Liu, Z. Wu, D. Yang, Y. Zheng, J. Peng, M. Feng, and D. Wang, "A new method for the electrostatic manipulation of droplet movement by triboelectric nanogenerator," Nano Energy **86**, 106115 (2021).
[19]Y. Chen and Y. Zheng, "Bioinspired micro-/nanostructure fibers with a water collecting property," Nanoscale **6**(14), 7703–7714 (2014).
[20]H. Dai, Z. Dong, and L. Jiang, "Directional liquid dynamics of interfaces with superwettability," Sci. Adv. **6**(37), eabb5528 (2020).
[21]H. Wang, Z. Xiang, P. Giorgia, X. Mu, Y. Yang, Z. L. Wang, and C. Lee, "Triboelectric liquid volume sensor for self-powered lab-on-chip applications," Nano Energy **23**, 80–88 (2016).
[22]R. Agapov, J. Boreyko, D. Briggs, B. Srijanto, S. Retterer, C. Collier, and N. Lavrik, "Asymmetric wettability of nanostructures directs Leidenfrost droplets," ACS Nano **8**(1), 860–867 (2014).
[23]Z. Jia, M. Chen, and H. Zhu, "Reversible self-propelled Leidenfrost droplets on ratchet surfaces," Appl. Phys. Lett. **110**, 091603 (2017).
[24]G. Lagubeau, M. Le Merrer, C. Clanet, and D. Quéré, "Leidenfrost on a ratchet," Nat. Phys. **7**(5), 395–398 (2011).
[25]J. Li, Y. Hou, Y. Liu, C. Hao, M. Li, M. K. Chaudhury, S. Yao, and Z. Wang, "Directional transport of high-temperature Janus droplets mediated by structural topography," Nat. Phys. **12**(6), 606–612 (2016).
[26]J. Li, X. Zhou, Y. Zhang, C. Hao, F. Zhao, M. Li, H. Tang, W. Ye, and Z. Wang, "Rectification of mobile Leidenfrost droplets by planar ratchets," Small **16**(9), e1901751 (2020).
[27]C. Lv and P. Hao, "Driving droplet by scale effect on microstructured hydrophobic surfaces," Langmuir **28**(49), 16958–16965 (2012).
[28]Y. Wang, R. Wang, Y. Zhou, Z. Huang, J. Wang, and L. Jiang, "Directional droplet propulsion on gradient boron nitride nanosheet grid surface lubricated with a vapor film below the Leidenfrost temperature," ACS Nano **12**(12), 11995–12003 (2018).
[29]P. Zhang, B. Peng, J. Wang, and L. Jiang, "Bioinspired self-propulsion of water droplets at the convergence of Janus-textured heated substrates," Adv. Funct. Mater. **29**(39), 1904535 (2019).
[30]B. Sobac, A. Rednikov, S. Dorbolo, and P. Colinet, "Self-propelled Leidenfrost drops on a thermal gradient: A theoretical study," Phys. Fluids **29**, 082101 (2017).
[31]H. Linke, B. J. Aleman, L. D. Melling, M. J. Taormina, M. J. Francis, C. C. Dow-Hygelund, V. Narayanan, R. P. Taylor, and A. Stout, "Self-propelled Leidenfrost droplets," Phys. Rev. Lett. **96**(15), 154502 (2006).
[32]D. Quéré, "Leidenfrost dynamics," Annu. Rev. Fluid Mech. **45**(1), 197–215 (2013).
[33]L. Scriven and C. Sternling, "The Marangoni effects," Nature **187**(4733), 186–188 (1960).
[34]G. Dupeux, T. Baier, V. Bacot, S. Hardt, C. Clanet, and D. Quéré, "Self-propelling uneven Leidenfrost solids," Phys. Fluids **25**, 051704 (2013).
[35]Y. Wang, A. El Bouhali, S. Lyu, L. Yu, Y. Hao, Z. Zuo, S. Liu, and C. Sun, "Leidenfrost drop impact on inclined superheated substrates," Phys. Fluids **32**, 112113 (2020).
[36]C. Liu, K. Sun, C. Lu, J. Su, L. Han, Z. Wang, and Y. Liu, "One-step process for dual-scale ratchets with enhanced mobility of Leidenfrost droplets," J. Colloid Interface Sci. **569**, 229–234 (2020).
[37]J. Xie, J. Xu, X. Li, and H. Liu, "Dropwise condensation on superhydrophobic nanostructure surface. I. Long-term operation and nanostructure failure," Int. J. Heat Mass Transfer **129**, 86–95 (2019).
[38]R. Cole, "Boiling nucleation," Adv. Heat Transfer **10**, 85–166 (1974).
[39]J. Salla, M. Demichela, and J. Casal, "BLEVE: A new approach to the superheat limit temperature," J. Loss Prev. Process Ind. **19**(6), 690–700 (2006).
[40]G. Castanet, O. Caballina, W. Chaze, R. Collignon, and F. Lemoine, "The Leidenfrost transition of water droplets impinging onto a superheated surface," Int. J. Heat Mass Transfer **160**, 120126 (2020).
[41]S. Lyu, V. Mathai, Y. Wang, B. Sobac, P. Colinet, D. Lohse, and C. Sun, "Final fate of a Leidenfrost droplet: Explosion or takeoff," Sci. Adv. **5**(5), eaav8081 (2019).
[42]Y. Utaka, T. Xie, Z. Chen, T. Morokuma, and H. Ohkubo, "Critical heat flux enhancement in narrow gaps via different-mode-interacting boiling with non-uniform thermal conductance inside heat transfer plate," Int. J. Heat Mass Transfer **133**, 702–711 (2019).
[43]H. Kim, B. Truong, J. Buongiorno, and W. Hu, "On the effect of surface roughness height, wettability, and nanoporosity on Leidenfrost phenomena," Appl. Phys. Lett. **98**, 083121 (2011).
[44] G. Lee, J. Kang, H. Park, K. Moriyama, S. Kim, and K. Kim, "Induced liquid-solid contact via micro/nano multiscale texture on a surface and its effect on the Leidenfrost temperature," Exp. Therm. Fluid Sci. **84**, 156–164 (2017).
[45]L. Zhong and Z. Guo, "Effect of surface topography and wettability on the Leidenfrost effect," Nanoscale. **9**, 6219–6236 (2017).
[46]A. Shati, S. Blakey, and S. Beck, "The effect of surface roughness and emissivity on radiator output," Energy Build. **43**, 400–406 (2011).
[47]X. Ji, J. Xu, H. Li, and G. Huang, "Switchable heat transfer mechanisms of nucleation and convection by wettability match of evaporator and condenser for heat pipes: Nano-structured surface effect," Nano Energy **38**, 313–325 (2017).
[48]S. Kandlikar, "A theoretical model to predict pool boiling CHF incorporating effects of contact angle and orientation," J. Heat Transfer **123**(6), 1071–1079 (2001).
[49]S. Kandlikar, "Evaporation momentum force and its relevance to boiling heat transfer," J. Heat Transfer **142**(10), 100801 (2020).
[50]H. Zhang, J. Xu, X. Zhu, J. Xie, M. Li, and B. Zhu, "The K number, a new analogy criterion number to connect pressure drop and heat transfer of sCO_2 in vertical tubes," Appl. Therm. Eng. **182**, 116078 (2021).
[51]B. Zhu, J. Xu, C. Yan, and J. Xie, "The general supercritical heat transfer correlation for vertical up-flow tubes: K number correlation," Int. J. Heat Mass Transfer **148**, 119080 (2020).
[52]A. Grounds, R. Still, and K. Takashina, "Enhanced droplet control by transition boiling," Sci. Rep. **2**, 720 (2012).
[53]A. Shahriari, P. S. Wilson, and V. Bahadur, "Acoustic detection of electrostatic suppression of the Leidenfrost state," Phys. Rev. E **98**(1), 013103 (2018).
[54]F. Celestini, T. Frisch, and Y. Pomeau, "Take off of small Leidenfrost droplets," Phys. Rev. Lett. **109**(3), 034501 (2012).
[55]X. Yan, J. Xu, Z. Meng, J. Xie, and H. Wang, "A new mechanism of light-induced bubble growth to propel microbubble piston engine," Small **16**(29), 2001548 (2020).
[56]M. Ishii and N. Zuber, "Drag coefficient and relative velocity in bubbly, droplet or particulate flows," AIChE J. **25**(5), 843–855 (1979).
[57]A. Bouillant, T. Mouterde, P. Bourrianne, A. Lagarde, C. Clanet, and D. Quéré, "Leidenfrost wheels," Nat. Phys. **14**, 1188–1192 (2018).
[58]V. Talari, P. Behar, Y. Lu, E. Haryadi, and D. Liu, "Leidenfrost drops on micro/nanostructured surfaces," Front. Energy **12**, 22–42 (2018).
[59]Q. Wang and R. Chen, "Ultrahigh flux thin film boiling heat transfer through nanoporous membranes," Nano Lett. **18**, 3096–3103 (2018).
[60]Y. Lin, F. Chu, Q. Ma, and X. Wu, "Gyroscopic rotation of boiling droplets," Appl. Phys. Lett. **118**, 221601 (2021).
[61]Z. Wu, W. Chang, and C. Sun, "A spherical Leidenfrost droplet with translation and rotation," Int. J. Therm. Sci. **129**, 254–265 (2018).
[62]See https://www.youtube.com/watch?v=aZZvq6ZR1Fo&ab_channel=LHU%E5%A4%9A%E5%AA%92%E9%AB%94%E7%89%B9%E6%95%88%E5%AF%A6%E9%A9%97%E5%AE%A4 for "High School Physics Collision Computer Animation" (last accessed September 20, 2015).